

New Diamond Magnet $\text{CaCo}_2\text{TeO}_6$: Strong Quantum Fluctuations and Enhanced Competing Exchange Interactions Enabled by Octahedral Co^{2+} Ligand Fields

Xudong Huai,¹ Luke Pritchard Cairns,² Bridget Delles,¹ Michał J. Winiarski,³ Maurice Sorolla II,⁴ Xinshu Zhang,⁵ Youzhe Chen,² Anshul Kogar,⁵ Robert Birgeneau,² James Analytis,² Stuart Calder,⁶ Danielle Yahne,⁶ Thao T. Tran*¹

Affiliations:

¹Department of Chemistry, Clemson University, Clemson, South Carolina 29634, United States

²Department of Physics, University of California, Berkeley, California, 94720, United States

³Faculty of Applied Physics and Mathematics and Advanced Materials Center, Gdansk University of Technology, 80-233 Gdansk, Poland

⁴Institute of Chemistry, University of the Philippines Diliman, Quezon City, Philippines

⁵Department of Physics and Astronomy, University of California, Los Angeles, California, 90095, United States

⁶Neutron Scattering Division, Oak Ridge National Laboratory, Oak Ridge, Tennessee 37830, United States

Abstract:

Diamond lattice magnets, formed by a framework of corner-sharing tetrahedra of magnetic cations, offer unique opportunities to realize novel states of matter for potential utility in information technology. However, research has mostly focused on AB_2X_4 spinels with T_d magnetic ions. This hinders the atomically enabled tunability of competing interactions at different energy scales and the ability to harness many-body electronic states in quantum materials, making the discovery of quantum fluctuations and spin dynamics less accessible. We discover a new material— $\text{CaCo}_2\text{TeO}_6$ —featuring a diamond lattice of two distinct $O_h\text{-Co}^{2+}$ sites. This material displays strong quantum fluctuations, increased competing magnetic exchange interactions, and field-induced tunability of magnetic structures. The results demonstrate how simple, fundamental refinements in ligand fields can profoundly influence the phase space of quantum matter.

Introduction

Developing information science and technology requires simple, fundamental approaches to engineer the energy levels of electronic spins in quantum systems. This can be achieved through intrinsic material properties (electronic structure, dimensionality, geometrical frustration, spin-orbit coupling, topology) and extrinsic perturbations (temperature, pressure, optics, and fields). (1-7) Diamond-lattice Heisenberg antiferromagnets, with their unique 3-D framework of corner-sharing tetrahedra of magnetic cations, provide a fascinating space for realizing novel states of matter. Elegant studies on diamond-lattice magnets have mainly focused on AB_2X_4 spinels, where

the magnetic A-site is placed in a tetrahedral ligand field (T_d) (Fig. 1a). (8-12) Examples include spin-liquid in MnSc_2S_4 , (13) spin-orbital entanglement in FeSc_2S_4 , (14) spin glass in CoAl_2O_4 , (15, 16) topological paramagnetism in NiRh_2O_4 , (17, 18) and an incommensurate spin helix in CuRh_2O_4 . Among spinels, $T_d\text{-Co}^{2+}$ diamond-lattice materials represent an exciting class of Heisenberg antiferromagnets. (19-27) Previous work showed that CoAl_2O_4 single crystals exhibit weak frustration and a spin-liquid state. CoGa_2O_4 was demonstrated to display spin glass behavior. (28) CoRh_2O_4 was realized as a conventional $S = 3/2$ diamond-lattice Heisenberg antiferromagnet with a long-range antiferromagnetic (AFM) ordering. Although the $T_d\text{-Co}^{2+}$ features, including significant spin-orbit coupling (SOC) of Co^{2+} (-527 cm^{-1}) (29) and a $J = 1/2$ ground state with SOC, could enable a realization of quantum effects in diamond magnets, it is a daunting task. This is in part attributable to three key reasons. First, nearest-neighbor AFM interactions dominate next-nearest-neighbor interactions, preventing the modulation of competing exchange interactions necessary for achieving a highly degenerate state. (30-34) Second, $T_d\text{-Co}^{2+}$ systems enter a $J = 3/2$ ground state in an applied magnetic field, derailing them from arriving at a field-induced $J = 1/2$ ground state (Fig. 1a). (35-40) Third, looking exclusively into spinels and related systems limits the tunability of spin states to a T_d ligand field alone, hindering the accessibility of quantum fluctuations in conventional diamond-lattice antiferromagnets. (8, 32, 41) Consequently, the ability to modify the energy landscape of electronic states and competing exchange interactions (nearest-neighbor and next-nearest-neighbor) in diamond-lattice magnets remains insufficiently understood, holding back our pursuit of quantum states in the presence or absence of external stimuli.

In this work, we make headway toward addressing this challenge by creating a new diamond magnet, $\text{CaCo}_2\text{TeO}_6$, with two distinct $O_h\text{-Co}$ sites (Fig. 1), in contrast to $T_d\text{-Co}$ in spinels. Careful solid-state synthesis and flux growth allow us to obtain crystals for further measurements. We characterize the structural and physical properties of the material using a series of probes including X-ray diffraction, magnetization, heat capacity, and neutron diffraction experiments. We place the interpretation of the data in context of other conventional diamond magnets and relevant systems. (42) We then supplement the experimental results with density functional theory calculations, linking the quantum-mechanical interference phenomena to the underlying chemistry and physics of the unique quantum properties of $\text{CaCo}_2\text{TeO}_6$.

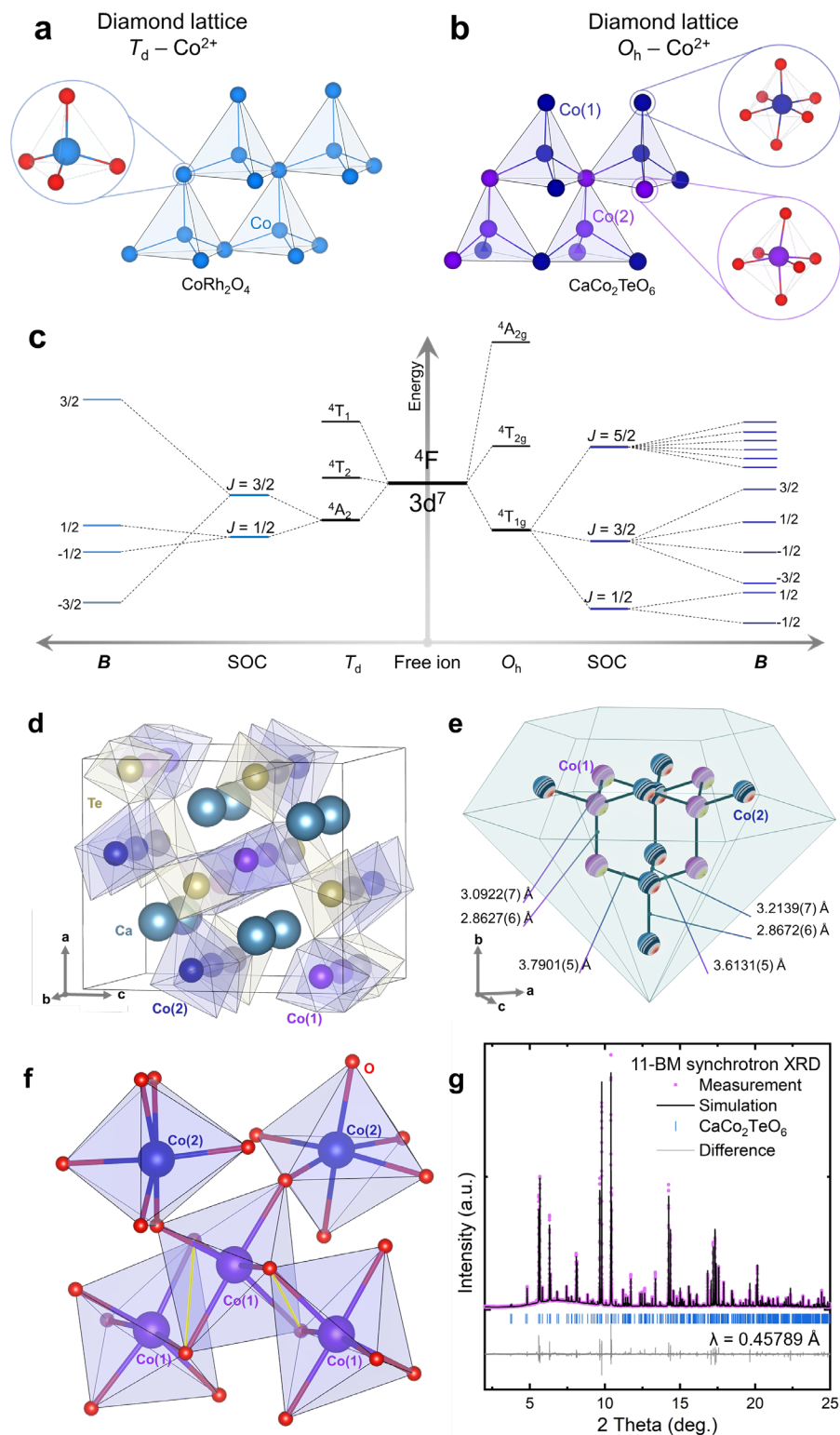


Fig. 1 Diamond lattice of (a) CoRh_2O_4 and (b) $\text{CaCo}_2\text{TeO}_6$. (c) Energy level diagram of T_d and O_h crystal field. (d) Crystal structures of $\text{CaCo}_2\text{TeO}_6$. (e) Magnetic sublattice of Co^{2+} , showing different Co-Co distances. (f) View showing magnetic exchange pathways through edge-sharing and corner-sharing $[\text{CoO}_6]$ octahedra. (g) Rietveld fit (black) of high-resolution synchrotron XRD data (purple) of $\text{CaCo}_2\text{TeO}_6$ and the difference between the experimental data and the simulation (grey).

Results and discussion

The crystal structure of $\text{CaCo}_2\text{TeO}_6$ was determined by in-lab single crystal X-ray diffraction (XRD) and confirmed by synchrotron powder XRD (11-BM Argonne National Laboratory) (Fig. 1d-g). $\text{CaCo}_2\text{TeO}_6$ crystallizes in the orthorhombic $Pnma$ space group and displays a 3-D diamond lattice of Co^{2+} with two crystallographically distinct Co(1) and Co(2) sites connected through CaO_6 and TeO_6 frameworks (Fig. 1b). Each Co^{2+} is bonded to six O atoms in a nearly perfect O_h coordination environment. The O_h local symmetry and the ${}^4T_{1g}$ ground state of the Co^{2+} ($3d^7$) ion are consistent with the electronic transitions observed in the UV-Vis-NIR spectra (Fig. S2) and further confirmed by SHG measurement (Fig. S3). The Co–O bonds range from 1.9808(2) Å to 2.1753(2) Å (Fig. 1c), shorter or close to that in a conventional diamond lattice (3.682 (2) Å in CoRh_2O_4)⁽³¹⁾ The variation of the Co–Co separation in $\text{CaCo}_2\text{TeO}_6$ originates from different fashions through which the CoO_6 octahedra are connected. Edge-sharing results in shorter Co–Co distances while corner-sharing leads to comparable Co–Co distances compared to those in CoRh_2O_4 , enabling the modulation of nearest and next-nearest neighbor exchange interactions (Fig. 1d). The new diamond lattice of $O_h\text{-Co}^{2+}$ in $\text{CaCo}_2\text{TeO}_6$ opens a previously untapped pathway to modify ground state degeneracy and competing energy scales in 3-D Heisenberg magnets.

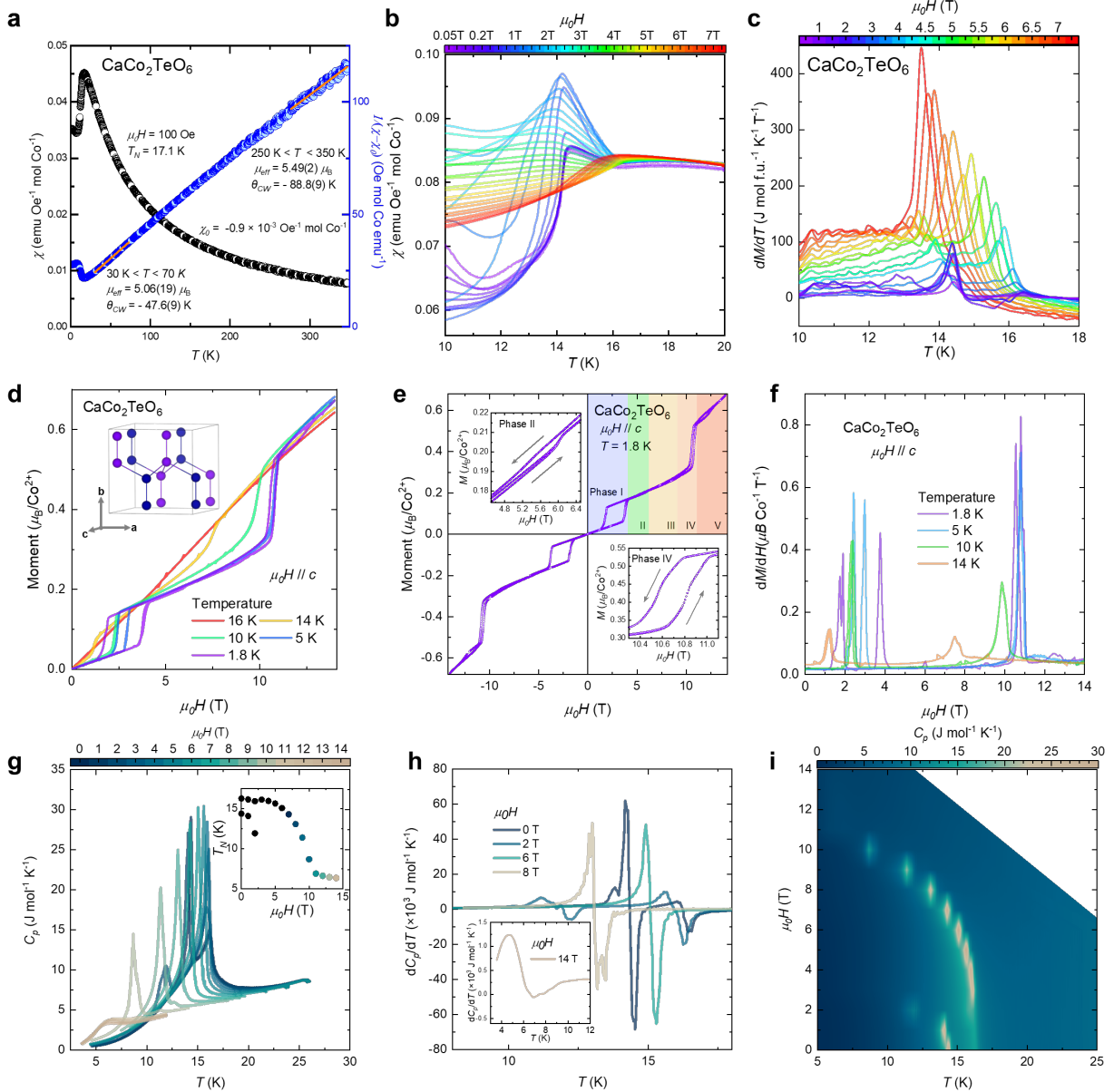


Fig. 2. (a) Magnetic susceptibility vs. temperature (black) and Curie-Weiss analysis (blue) at $\mu_0H = 100$ Oe. (b) Temperature-dependent magnetic susceptibility under different magnetic fields. (c) First derivative of magnetization with respect to temperature under magnetic field. (d) Magnetic moment as a function of applied field $\mu_0H \parallel c$ at different temperatures. (e) $M(H)$ curve at $T = 1.8$ K showing field-induced tunability of magnetic phases. (f) First derivative of $M(H)$ at $\mu_0H \parallel c$ and different temperatures. (g) Heat capacity showing two anomalies suppressed to lower temperature at high fields and evolving into one broad hump; insert showing the magnetic transition temperature as a function of applied field. (h) Derivative dC_p/dT showing the evolution of magnetic transitions with fields. (i) A map of heat capacity as a function of temperature and field showing the progression of magnetic transitions.

To probe the magnetic interactions in $\text{CaCo}_2\text{TeO}_6$, we turned to magnetization measurements as a function of temperature and field. This material undergoes antiferromagnetic (AFM) transitions at $T_{N1} = 17.1$ and $T_{N2} = 15.5$ K at $\mu_0H = 0.01$ T, clearly revealed by two anomalies in the dM/dT curves (Fig. 2a-c). The transition temperature is decreased at higher applied fields (Fig. S4). At $T > T_N$, the inverse magnetic susceptibility is well described by the Curie-Weiss law for

the paramagnetic regime. At low field $\mu_0H = 0.01$ T (Fig. 2a), Curie-Weiss temperatures θ_{CW} of -47.6(9) K ($30 \text{ K} \leq T \leq 70 \text{ K}$) and -88.8(9) K ($250 \text{ K} \leq T \leq 350 \text{ K}$) indicate a net AFM interaction in the $O_h\text{-Co}^{2+}$ diamond magnet. The effective magnetic moment μ_{eff} per Co^{2+} ion is $\mu_{\text{eff}} = 5.1(1)$ and $5.5(1) \mu_B$ at $30 \text{ K} \leq T \leq 70 \text{ K}$ and $250 \text{ K} \leq T \leq 350 \text{ K}$, respectively, close to the expected value considering spin-orbit coupling: $4.74 \mu_B$ for $S = 3/2$ and $L = 1$ and $5.67 \mu_B$ for $S = 3/2$ and $L = 2$. This result agrees with $J_{\text{eff}} = 1/2$ ground state due to Kramers doublet at low temperature.(38, 43, 44) The effective g -factor was extracted from the Curie constant to be $g_{\text{eff}} = 2.24$, greater than the electron-spin $g_e = 2$, confirming the significant orbital contribution in the $O_h\text{-Co}^{2+}$ diamond magnet. At high $\mu_0H = 7$ T (Fig. S4b), the effective magnetic moment extracted from the Curie-Weiss analysis is $\mu_{\text{eff}} = 6.8 \mu_B$ per Co^{2+} ion, close to the expected value $6.6 \mu_B$ for $S = 3/2$ and $L = 3$. This reveals the significant orbital contribution to magnetism and field-driven tunability of magnetic states.(45) Fig. 2c depicts how the magnetization of the material evolves under different fields near T_N . The magnetic susceptibility (Fig. 2b) shows a transition at $T_{N1} = 16$ K, followed by an antiferromagnetic transition at $T_{N2} = 14.5$ K. Upturns and downturns in the $\chi(T)$ curves suggest competing FM and AFM interactions. As magnetic fields increase, the two magnetic transitions are suppressed to lower temperatures and then evolve into only one transition observed at $\mu_0H > 4$ T. This behavior is also clearly shown in the dM/dT curves in which ridges can imply field-induced transitions (Fig. 2c). Upturns in the $\chi(T)$ curves at $T < 12$ K can be attributed to competition between nearest-neighbor and next-nearest-neighbor Co-Co interactions, similar to that in $T_d\text{-Co}^{2+}$ diamond lattices in spinels.(18, 31) However, the competing interactions (Table S2) of the $O_h\text{-Co}^{2+}$ spins in $\text{CaCo}_2\text{TeO}_6$ are more complex than those in $T_d\text{-Co}^{2+}$ diamond magnets since there are six nearest-neighbor Co-Co interactions through Co(1)-Co(1), Co(2)-Co(2), and Co(1)-Co(2). Orientation-dependent isothermal magnetization $M(H)$ curves display strong magnetic anisotropy (Fig. S5), which decreases with increasing temperature. The $M(H)$ curves with $\mu_0H // a$ show linear correlation while those with $\mu_0H // b$ and c feature hysteresis loops at $T = 10, 5, \text{ and } 1.8 \text{ K} < T_{N1,2}$. The hysteresis loops have zero coercivity and dumbbell shapes (Fig. 2d-f). While the net magnetic interactions in $\text{CaCo}_2\text{TeO}_6$ are dominated by AFM exchange, the double hysteresis loops indicate FM spin correlations. At $T = 16$ K, the hysteresis corresponding to FM exchange vanishes but metamagnetic transitions are still observed. Similar double hysteresis loops have been reported for $\text{BaCo}_2(\text{AsO}_4)_2$ honeycomb.(46-49) No frequency dependence is observed in the AC magnetization data under different fields (Fig. S6), indicating no spin-freezing transition. The isothermal magnetic entropy change is derived from the Maxwell relation (Equation 1):

$$\left(\frac{dS}{dH}\right)_T = \left(\frac{dM}{dT}\right)_H \quad (1)$$

where S is the entropy, M is the magnetization, T is the temperature, and H is the magnetic field. The magnetic entropy can be extracted from Equation 2:

$$\Delta S_{\text{mag}}(H, T) = \int_0^H \left(\frac{dM}{dT}\right)_{H'} dH' \quad (2)$$

Fig. S7 shows the $\Delta S_{\text{mag}}(H, T)$ map of $\text{CaCo}_2\text{TeO}_6$ under a series of applied magnetic fields $0.01 \text{ T} \leq \mu_0H \leq 7 \text{ T}$ around the transition temperatures. At $\mu_0H \geq 6 \text{ T}$ and $15 \text{ K} \leq T \leq 16 \text{ K}$, a red region of positive entropy of approximately $1.5 \text{ J mol}^{-1} \text{ K}^{-1}$ is observed, indicative of a possible formation of topologically nontrivial phases. The field-induced magnetic transitions are further confirmed by specific heat measurements.

The temperature-dependent heat capacity data at $0 \text{ T} \leq \mu_0 H \leq 14 \text{ T}$ around the transition temperatures are presented in Fig. 2g-i. At $0 \text{ T} \leq \mu_0 H \leq 4 \text{ T}$, two peaks are observed in the $C_p(T)$ curves, denoting the two magnetic phase transitions as seen in the magnetization data. As the magnetic field increases, the sharp peaks at T_{N1} and T_{N2} shift to lower temperatures and become broader. At $4 \text{ T} \leq \mu_0 H \leq 14 \text{ T}$, these peaks evolve into one, which is eventually suppressed at $\mu_0 H > 10 \text{ T}$. This indicates that the magnetic ordering is suppressed and the $O_h\text{-Co}^{2+}$ diamond system enters into a quantum fluctuation state with short-range spin correlations at high fields. Similar field-driven quantum spin liquid or spin dynamics states have been observed in 2-D honeycomb magnets $\alpha\text{-RuCl}_3$, $\text{BaCo}_2(\text{AsO}_4)_2$ and $\text{Na}_2\text{Co}_2\text{TeO}_6$.(49-55). This similarity may stem from the honeycomb magnets and the $O_h\text{-Co}^{2+}$ diamond magnet possessing bipartite lattices that enable competing nearest-neighbor and next-nearest-neighbor interactions (Fig. S8). While some degree of perturbation of magnetic ordering has been observed in $T_d\text{-Co}^{2+}$ diamond lattices in spinels, the realization of the field-induced quantum spin fluctuations is unique for the $O_h\text{-Co}^{2+}$ diamond magnet $\text{CaCo}_2\text{TeO}_6$.

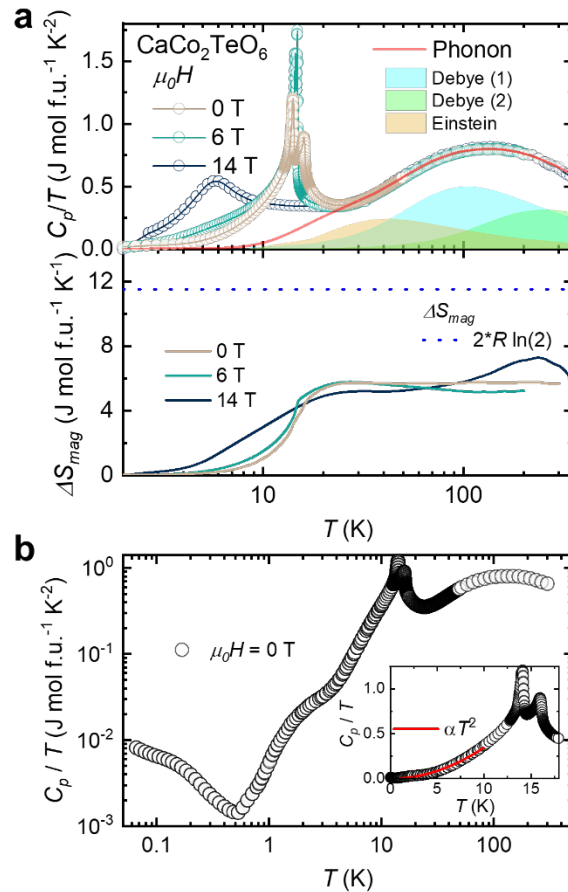


Fig. 3. (a) Molar heat capacity over temperature (C_p/T) vs. temperature for $\text{CaCo}_2\text{TeO}_6$ at $\mu_0 H = 0 \text{ T}$ and calculated phonon (red). The anomalies are consistent with the magnetic phase transitions of the material. Magnetic entropy change (ΔS_{mag}) at different magnetic fields (solid lines) compared to the expected value of $J_{\text{eff}} = 1/2$ spins ($2R \ln 2$) (dash line). (b) Low-temperature heat capacity of $\text{CaCo}_2\text{TeO}_6$ showing the onset of the nuclear quadrupole Schottky Co at $0.06 \text{ K} \leq T \leq 0.4 \text{ K}$.

Fig. 3 presents the heat capacity as a function of temperature $0.1 \text{ K} \leq T \leq 300 \text{ K}$ at $\mu_0 H = 0 \text{ T}$ and phonon and magnetic entropy ΔS_{mag} analysis. The magnetic entropy change ΔS_{mag} can be calculated from Equation 3:

$$\Delta S = \int_0^T \frac{C_v}{T} dT \quad (3)$$

where C_v is the heat capacity at constant volume, which is approximated to be C_p (heat capacity at constant pressure) for solids at low temperatures, and T is the temperature. Extracting the magnetic contribution to the heat capacity requires a reliable phonon subtraction using a most direct nonmagnetic isostructural analog or a phonon model. We attempted to prepare the unknown $\text{CaZn}_2\text{TeO}_6$ as the nonmagnetic version for subtracting the lattice contribution but were not successful. Thus, we constructed a phonon model that best describes the high-temperature heat capacity data by using two Debye modes and one Einstein model as follows (Equation 4):

$$\frac{C_p}{T} = \frac{C_{\text{Debye}(1)}}{T} + \frac{C_{\text{Debye}(2)}}{T} + \frac{C_{\text{Einstein}(1)}}{T} \quad (4)$$

$$C_{\text{Debye}} = 9NRs_D \left(\frac{T}{\Theta_D}\right)^3 D(\Theta_D/T) \quad (5)$$

$$C_{\text{Einstein}} = 3NRs_E \frac{(Q_E/T)^2 \exp(Q_E/T)}{[\exp(Q_E/T) - 1]^2} \quad (6)$$

where N represents the number of atoms, R is the gas constant, T is the sample temperature, s_D is the number of oscillators of acoustic phonon, Θ_D is the Debye temperature, $D(\Theta_D/T)$ is the Debye function, s_E is the number of oscillators of optical phonon, and Θ_E is the Einstein temperature. The model parameters from the fitting are summarized in Table S5. Our assessment of the two-Debye one-Einstein phonon model is based on the resulting good fit and physical oscillator terms. It is rationalized by the three subunits: the phonon modes of (i) the magnetic sublattice, (ii) the nonmagnetic sublattice, and (iii) the counteraction site in the structure framework. The total number of oscillators is 9.7(5) (Table S5), close to the total number of 10 atoms in the formula unit for $\text{CaCo}_2\text{TeO}_6$. After subtracting the phonon contribution, the magnetic heat capacity under different fields C_{mag}/T vs. T was integrated to obtain the entropy change associated with the magnetic ordering. Fig. 3a presents the magnetic entropy change ΔS_{mag} reaches a maximum of 5.7(1) J mol f.u.⁻¹ K⁻¹ above $T_{N1,2}$. A material consisting of two Co^{2+} ions with $J_{\text{eff}} = 1/2$ should have a magnetic entropy change of $2 * R \ln(2) = 11.52 \text{ J mol f.u.}^{-1} \text{ K}^{-1}$. The observed ΔS_{mag} is only $\sim 1/2$ of the expected value for $J_{\text{eff}} = 1/2$ at $\mu_0 H \leq 14 \text{ T}$. The missing entropy can be attributed to three possible reasons. First, the two-Debye one-Einstein phonon model overestimates the lattice contribution. Second, additional entropy below $T = 2 \text{ K}$ is not successfully captured by a linear extrapolation of C_p/T reaching 0 at $T = 0 \text{ K}$. Third, potential quantum fluctuations and short-range correlations are present in $\text{CaCo}_2\text{TeO}_6$. The field-induced magnetic entropy change ΔS_{mag}^H can be extracted by taking the difference between $\Delta S(\mu_0 H, T)$ and $\Delta S(0, T)$ (Fig. S7 c, d). A positive peak ΔS_{mag}^H implies a high entropy magnetic state, whereas a negative peak denotes a long-range magnetic ordering. The evolution of positive and negative peaks ΔS_{mag}^H as a function of temperature at different magnetic fields confirms the rich magnetic properties of the $O_h\text{-Co}^{2+}$ diamond magnet, consistent with the magnetization data. As the magnetic field increases, the long-range magnetic ordering (negative peak) is suppressed and transitions into a high entropy magnetic

state. This indicates the presence of strong quantum fluctuations at high fields, in concert with the magnetization data. Fig. 3b presents an upturn in the low-temperature heat capacity at $0.06 \text{ K} \leq T \leq 0.4 \text{ K}$, which is too low in energy and magnitude to be assigned as a magnetic phase transition. So, it is most likely to be attributed to the nuclear quadrupole Schottky from Co, however, the Schottky anomaly is expected to be around 10^{-3} K .(56) While the observed Schottky tail does not supply sufficient information to be extracted for the nuclear quadrupole Schottky of Co, it proves the realization of quantum fluctuations down to $T = 0.06 \text{ K}$. The heat capacity below T_N ($0.5 \text{ K} < T < 10 \text{ K}$) follows a $C_p = \alpha T^3$ behavior (Fig. 3b insert), which is expected for gapless antiferromagnetic magnons.(31)

To gain more insight into how the electronic structure of $\text{CaCo}_2\text{TeO}_6$ manifests its physical properties, full-potential spin-polarized DFT calculations were performed using WIEN2k (57)(Fig. S9). The bands around the Fermi level (E_F) are diffused, indicating appreciable overlap between the Co- d and O- p states and covalent bonding features. The spins of the Co- d states are polarized and further polarize the O- p , Te- s/p , and Ca- s states, suggesting magnetic interactions along different directions. The valence band maximum and conduction band minimum primarily consist of the Co- d and O- p states. This indicates sizable interactions between Co-O-Co. Thus, the DFT results supplement the rich magnetic behavior of the material while appreciating the presence of competing magnetic exchange interactions of nearest-neighbor and next-nearest-neighbor in the O_h - Co^{2+} diamond magnet.

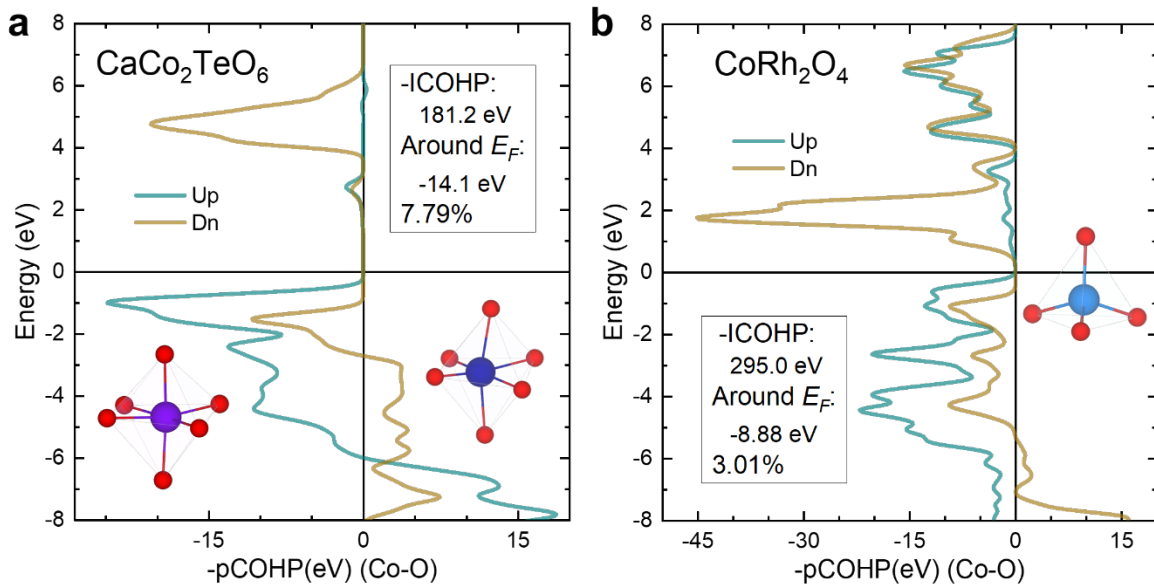


Fig. 4. Projected crystal orbital Hamilton population (pCOHP) with their integrated value (ICOHP) showing some level of electronic instabilities around E_F .

To gain more insights into how chemical bonding in O_h - $[\text{CoO}_6]$ in the diamond magnet $\text{CaCo}_2\text{TeO}_6$ can facilitate competing magnetic exchange interactions and how it is compared to T_d - $[\text{CoO}_4]$ in the conventional diamond magnet CoRh_2O_4 , additional pseudo potential DFT calculations were performed by utilizing the projector-augmented wave (PAW) method implemented in the Quantum Espresso (58) and projected into a linear combination of atomic

orbital (LCAO) using LOBSTER (59, 60) software packages. The spin-polarized DOS curves from the pseudopotential calculations (Fig. S10) are similar to those from full-potential (Fig. S9), validating the DFT results. To know more about the phase information of the orbitals involved in the overlap of the atomic interacting wavefunctions, the projected crystal orbital Hamilton population (-pCOHP) was extracted (61, 62). The -pCOHP curves for O_h -[CoO₆] and T_d -[CoO₄] (Fig. S13, 14) clearly show Co-O antibonding characters, as proposed in Fig. S1. In Fig. S12, the total integrated Co-O COHPs up to E_F (ICOHPs) show overall bonding strength for O_h -[CoO₆] in CaCo₂TeO₆ and T_d -[CoO₄] in CoRh₂O₄. For O_h -[CoO₆], the total Co-O interaction strengths are similar in magnitude, and overall, the Co(1)-O bonds are slightly stronger than the Co(2)-O bonds. For T_d -[CoO₄] (Fig. S12b), the Co-O bonds feature the same strength due to symmetry. To appreciate the electronic instability difference around E_F , we integrated the pCOHP of the Co-*d* and O-*p* orbitals within each O_h -[CoO₆] and T_d -[CoO₄] cluster up to E_F per unit cell, the energy scale is determined from the DOS curve (Fig. S14). The ICOHP values (Fig. 4) around E_F are then compared to the total ICOHP in a unit cell of each compound to quantify the electronic instability. The results show that O_h -[CoO₆] in CaCo₂TeO₆ displays larger electronic instability (7.79%) compared to T_d -[CoO₄] in CoRh₂O₄ (3.01%), suggesting that access to exotic states of matter in the O_h -Co²⁺ diamond magnet is more accessible than in conventional diamond magnets.

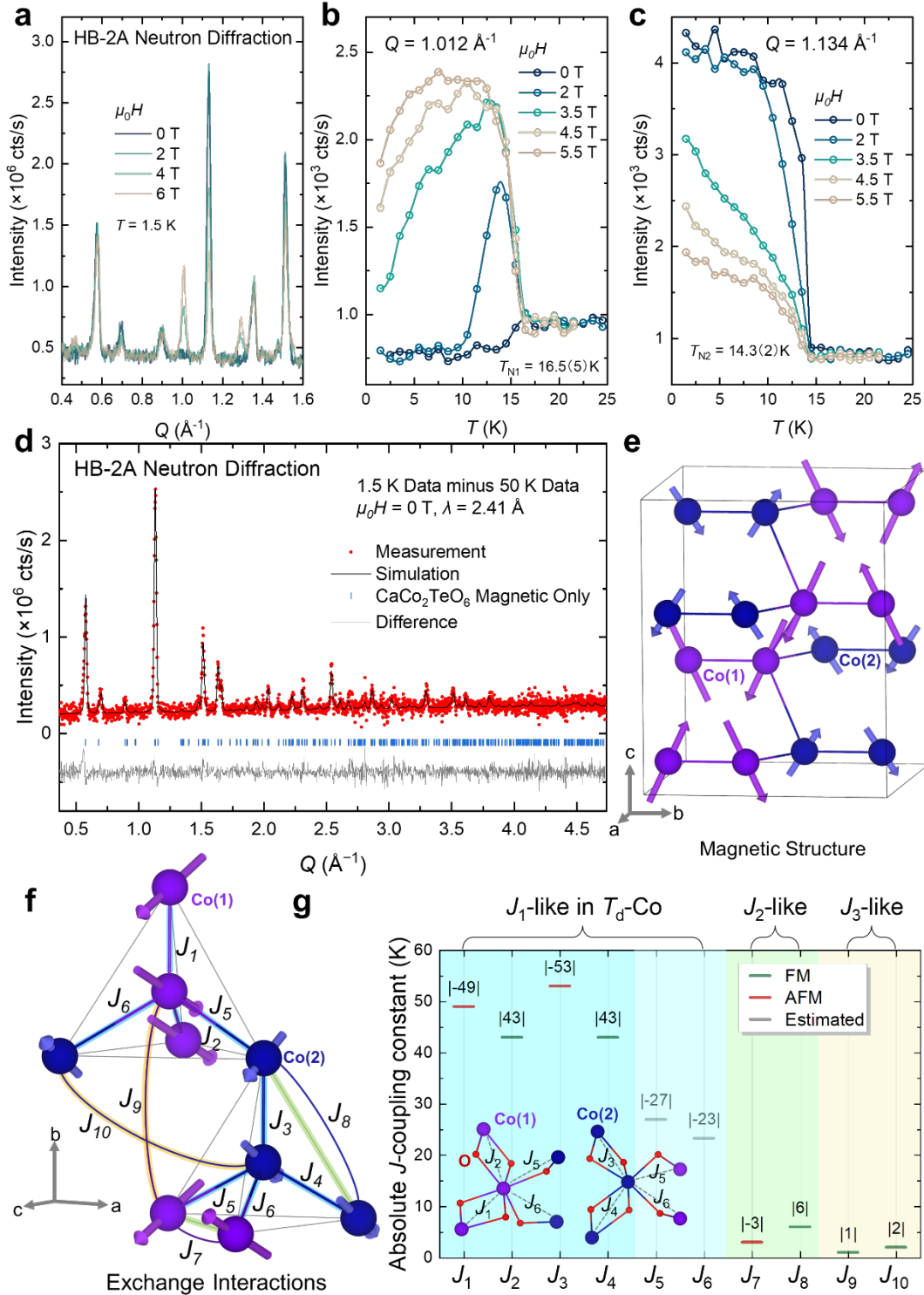


Fig. 5. (a) HB-2A powder neutron diffraction of $\text{CaCo}_2\text{TeO}_6$ at a wavelength of 2.41 \AA under different fields at $T = 1.5$ K. (b) Evolution of the intensity of the magnetic Bragg peaks at $Q = 1.012 \text{ \AA}^{-1}$ at $1.5 \text{ K} \leq T \leq 25 \text{ K}$ under different fields, showing the Neel temperature of $T_{N1} = 16.5(5)$ K (c) The intensity of the most intense magnetic Bragg peaks at different fields showing the Neel temperature of $T_{N2} = 14.3(2)$ K. (d) Magnetic structure refinement. (e) Refined magnetic structure with the propagation vector $\mathbf{q} = (0, 0, 0)$. (f) J -coupling interactions in $\text{CaCo}_2\text{TeO}_6$. (g) Calculated J -coupling constants.

To investigate the magnetic ground state associated with this electronic instability, neutron diffraction measurements were conducted on HB-2A powder at Oak Ridge National Laboratory. The diffraction patterns (Fig. 5a-c) reveal strong temperature- and field-dependent behaviors, corroborating the magnetic phase diagram determined from heat capacity, magnetic susceptibility, and magnetization discussed above. Specifically, the magnetic Bragg peak at $Q = 1.012 \text{ \AA}^{-1}$ only present upon applied fields and the intensity increases with magnetic field and temperature below the Néel temperature ($T_N = 15.5 \text{ K}$). In contrast, the intensity of the strongest magnetic Bragg peak at $Q = 1.134 \text{ \AA}^{-1}$ decreases with applied field and temperature under T_N , confirming an ordering temperature of $16.5(5) \text{ K}$ at $\mu_0 H = 0 \text{ T}$ and $13.5(5) \text{ K}$ at $\mu_0 H = 5.5 \text{ T}$. In zero-field, magnetic Bragg peaks emerged below $T_N = 14 \text{ K}$ (Fig 5c) that can be indexed to a $k = 0$ magnetic propagation vector. In addition, a small, yet distinct, intermediate phase emerged briefly between $14 < T < 16 \text{ K}$. The propagation vector of the intermediate phase seems to be temperature-dependent but can be nearly indexed to $\mathbf{k} = (0 \frac{1}{4} 0)$. However, the exact structure of the intermediate phase cannot be determined from powder neutron diffraction alone, as the fit is severely under-constrained. Instead, future single-crystal neutron diffraction will be necessary to unravel the nature of the intermediate phase. As field is applied, new peaks emerge (Fig 5b), possibly related to the intermediate phase, given their temperature dependence. The nature of these field-induced phases is still under investigation.

The nuclear and magnetic structures were refined using FullProf (63) and TOPAS software (64, 65) (Fig. 5d, S18). At $T = 1.5 \text{ K}$ and $\mu_0 H = 0 \text{ T}$, the resulting magnetic peaks can be indexed by a single propagation vector, $\mathbf{k}_m = (0, 0, 0)$, with respect to the conventional unit cell. This corresponds to a magnetic structure in the $Pnma$ (No. 62.441) magnetic space group (Γ_1 irreducible representation) and produces two distinct magnetic moments for each type of Co ion (Table S6, 7, 8). The resulting structure is a noncollinear AFM with the moment constrained within the bc -plane. We note that a small out-of-plane (a -axis) moment, around $0.3 \mu_B$, could be included without drastically changing the goodness-of-fit. Co(1) and Co(2), aligned approximately 56° and 64° , respectively, from the b -axis (Table S6). The refined magnetic moment of Co(1) is $3.03(1) \mu_B$, $\sim 10\%$ lower than the expected magnetic moment of $\mu_{\text{cal}} = gS = 3.36 \mu_B$ (where $S = 3/2$ and $g_{\text{eff}} = 2.24$). Additionally, the magnetic moment for Co(2) is found to be $2.15(1) \mu_B$, approximately 36% lower than the expected value. The appreciable reduction in the static moment on both the Co(1) and Co(2) sites indicates the presence of strong quantum fluctuations in $\text{CaCo}_2\text{TeO}_6$. Similar quantum effects have been observed in ZnCr_2Se_4 pyrochlore with $S = 3/2$, (66, 67) and in CuAl_2O_4 diamond magnet with $S = 1/2$. (68, 69) However, it is rare to observe such sizable quantum fluctuations in conventional diamond magnets with a relatively large spin system ($S = 3/2$).

To better understand the magnetic interactions that give rise to this noncollinear magnetic ground state and strong quantum fluctuations (Fig. 5f), we performed additional DFT calculations to extract the J -coupling constants while validating multicenter Co-O-Co interactions through crystal orbital bond index (COBI) analysis (Fig. S19e). (70) The integrated COBI (ICOBI) implies that the interactions between the same Co types Co(1)-O-Co(1) (J_{1-2}) and Co(2)-O-Co(2) (J_{3-4}) surpass those between different Co types Co(1)-O-Co(2) ($J_{5,6}$). To account for the direct Co-Co interactions, we calculated the COHP between Co atoms within a tetrahedron (Fig. S19f). The ICOHP (Fig. S19f) confirms that the interaction between Co(1)-Co(1) (3.09 \AA) is stronger than that of Co(1)-Co(2) (3.61 \AA). To quantify the Co-Co magnetic exchange interactions in $\text{CaCo}_2\text{TeO}_6$, we applied Green's function method by using the Wannier formalism through DFT and the Heisenberg model. (71) The nearest-neighbor magnetic exchange interactions J_{1-4} occurring between the same Co types through two edge-sharing O_h -[CoO_6] were identified to be $J_1 = -49 \text{ K}$

(AFM), $J_2 = 43$ K (FM), $J_3 = -53$ K (AFM) and $J_4 = 43$ K (FM)(Fig. 5f). This calculated result aligns very well with the magnetic structure determined from the neutron experiments. The next-nearest-neighbor magnetic exchange interactions mediated by one corner-sharing O_h -[CoO₆] were estimated to be $J_5 = -27$ K (AFM) and $J_6 = -23$ K (AFM), in the same order of magnitude as the nearest-neighbor interactions J_{1-4} . The strong competing AFM-FM nearest-neighbor and next-nearest-neighbor exchange interactions at a similar energy scale may facilitate the observed quantum fluctuations.⁽⁷²⁻⁷⁴⁾ The second-nearest-neighbor exchange interactions J_{7-8} are about 1/8 of J_{1-6} , whereas the third-nearest-neighbor interactions J_{9-10} are negligible. This is similar to what has been observed in conventional diamond magnets. ^(16, 32) While the magnetic exchange interactions in CaCo₂TeO₆ share some common features with those in conventional diamond magnets, the strong competing AFM-FM coupling constants and unique exchange pathways in the O_h -Co²⁺ diamond magnet enabled by an octahedral ligand field offer a new avenue to realize quantum fluctuations.

Conclusions

The results enable a new pathway to reimagine the ligand-field-enabled modulation of quantum fluctuations and spin dynamics in geometrically frustrated magnets. Through careful flux growth and solid-state synthesis, we create a new diamond magnet, CaCo₂TeO₆, wherein two distinct Co²⁺ ions experience an octahedral ligand field—a feature that was previously untapped. This complements the current stage-of-the-art of conventional spinel diamond magnets having a magnetic ion placed in a tetrahedral ligand field. While CaCo₂TeO₆ displays some shared features with conventional diamond magnets, the material offers a discovery of field-induced tunability of magnetic states, magnetic anisotropy, strong competing AFM-FM exchange interactions, and appreciable quantum fluctuations down to $T = 0.06$ K. The two AFM magnetic orders are suppressed to lower temperatures at high fields and then evolve into one, which is further suppressed at $\mu_0 H > 10$ T. Although the net magnetic interactions in the O_h -Co²⁺ diamond magnet are dominated by AFM exchange, the double hysteresis loops in $M(H)$ reveal competing FM spin correlations. The material displays a noncolinear AFM magnetic ground state and an appreciable reduction in the magnetic moment on both Co sites, confirming strong quantum fluctuations. Our DFT calculations result in sizable covalent Co-O bonding characters and increased electronic instability while acknowledging the strong competing AFM-FM nearest-neighbor and next-nearest-neighbor magnetic exchange interactions at a comparable energy scale. The enhanced competing exchange interactions are attributable to the new coupling pathways—combined edge-sharing and corner-sharing [CoO₆] octahedra—in the O_h -Co²⁺ diamond magnet. Our work demonstrates a simple, fundamental framework of using ligand fields to atomically modify the energy landscape of many-body electronic states and competing magnetic exchange interactions, enabling the realization of strong quantum fluctuations, spin dynamics, and other potential novel states of matter.

Acknowledgments:

XH and TTT thank Dr. C. McMillen, Dr. R. Sachdeva, and Dr. Matthew Powell for their assistance in X-ray diffraction, TGA, and some physical property measurements. A portion of this research used resources at the High Flux Isotope Reactor, a DOE Office of Science

User Facility operated by the Oak Ridge National Laboratory. Use of the Advanced Photon Source at the Argonne National Laboratory was supported by the U.S. Department of Energy, Office of Science, Office of Basic Energy Sciences, under Contract No. DE-AC02-06CH11357. This manuscript was authored by UT-Batelle, LLC, under contract DE-AC05-00OR22725 with the US Department of Energy (DOE). The US government retained and the publisher, by accepting the article for publication, acknowledged that the US government retained a nonexclusive, paid-up, irrevocable, worldwide license to publish or reproduce the published form of this manuscript, or allowed others to do so, for US government purposes. DOE would provide public access to these results of federally sponsored research in accordance with the DOE Public Access Plan (<http://energy.gov/downloads/doe-public-access-plan>).

Funding:

Arnold and Mabel Beckman Foundation grant 2023 BYI (XH, BD, TTT)

National Science Foundation grants NSF-DMR-CAREER-2338014 and NSF-OIA-2227933 (XH, BD, TTT)

References

1. Y. Zhou, K. Kanoda, T.-K. Ng, Quantum spin liquid states. *Reviews of Modern Physics* **89**, 025003 (2017).
2. C. Broholm *et al.*, Quantum spin liquids. *Science* **367**, eaay0668 (2020).
3. J. R. Chamorro, T. M. McQueen, T. T. Tran, Chemistry of quantum spin liquids. *Chemical Reviews* **121**, 2898-2934 (2020).
4. A. Chauhan *et al.*, Quantum spin liquids on the diamond lattice. *arXiv preprint arXiv:2306.12032*, (2023).
5. S. Nakatsuji *et al.*, Spin disorder on a triangular lattice. *science* **309**, 1697-1700 (2005).
6. A. D. King, C. Nisoli, E. D. Dahl, G. Poulin-Lamarre, A. Lopez-Bezanilla, Qubit spin ice. *Science* **373**, 576-580 (2021).
7. S. Nakatsuji *et al.*, Spin-orbital short-range order on a honeycomb-based lattice. *Science* **336**, 559-563 (2012).
8. D. G. Wickham, J. B. Goodenough, Suggestion concerning magnetic interactions in spinels. *Physical Review* **115**, 1156 (1959).
9. R. M. Hazen, Comparative compressibilities of silicate spinels: anomalous behavior of (Mg, Fe)₂SiO₄. *Science* **259**, 206-209 (1993).
10. N. Tristan *et al.*, Geometric frustration in the cubic spinels MA₂O₄ (M = Co, Fe, and Mn). *Physical Review B* **72**, 174404 (2005).
11. N. Mufti, A. A. Nugroho, G. R. Blake, T. T. M. Palstra, Magnetodielectric coupling in frustrated spin systems: the spinels MCr₂O₄ (M = Mn, Co and Ni). *Journal of physics: Condensed matter* **22**, 075902 (2010).
12. O. Zaharko, A. Cervellino, V. Tsurkan, N. B. Christensen, A. Loidl, Evolution of magnetic states in frustrated diamond lattice antiferromagnetic Co(Al_{1-x}Co_x)₂O₄ spinels. *Physical Review B* **81**, 064416 (2010).

13. V. Fritsch *et al.*, Spin and orbital frustration in MnSc_2S_4 and FeSc_2S_4 . *Physical review letters* **92**, 116401 (2004).
14. V. Fritsch *et al.*, Spin and orbital frustration in MnSc_2S_4 and FeSc_2S_4 . *Physical review letters* **92**, 116401 (2004).
15. B. C. Melot *et al.*, Magnetic frustration on the diamond lattice of the A-site magnetic spinels $\text{CoAl}_{2-x}\text{Ga}_x\text{O}_4$: The role of lattice expansion and site disorder. *Physical Review B* **80**, 104420 (2009).
16. O. Zaharko *et al.*, Spin liquid in a single crystal of the frustrated diamond lattice antiferromagnet CoAl_2O_4 . *Physical Review B* **84**, 094403 (2011).
17. F. L. Buessen, M. Hering, J. Reuther, S. Trebst, Quantum spin liquids in frustrated spin-1 diamond antiferromagnets. *Physical review letters* **120**, 057201 (2018).
18. J. R. Chamorro *et al.*, Frustrated spin one on a diamond lattice in NiRh_2O_4 . *Physical Review Materials* **2**, 034404 (2018).
19. K. W. Plumb *et al.*, Antiferromagnetic and orbital ordering on a diamond lattice near quantum criticality. *Physical Review X* **6**, 041055 (2016).
20. S. Marik *et al.*, Enhanced magnetic frustration in a new high entropy diamond lattice spinel oxide. *Scripta Materialia* **186**, 366-369 (2020).
21. M. E. Zhitomirsky, Enhanced magnetocaloric effect in frustrated magnets. *Physical Review B* **67**, 104421 (2003).
22. A. P. Ramirez, Strongly geometrically frustrated magnets. *Annual Review of Materials Science* **24**, 453-480 (1994).
23. L. Balents, Spin liquids in frustrated magnets. *nature* **464**, 199-208 (2010).
24. H.-K. Jin, W. M. H. Natori, F. Pollmann, J. Knolle, Unveiling the $S=3/2$ Kitaev honeycomb spin liquids. *Nature communications* **13**, 3813 (2022).
25. S. Gao *et al.*, Fractional antiferromagnetic skyrmion lattice induced by anisotropic couplings. *Nature* **586**, 37-41 (2020).
26. V. Tsurkan *et al.*, Ultra-robust high-field magnetization plateau and supersolidity in bond-frustrated MnCr_2S_4 . *Science advances* **3**, e1601982 (2017).
27. C. Broholm *et al.*, *c. Science* **367**, eaay0668 (2020).
28. J. Hu, Y. Ma, X. Kan, C. Liu, Observation of spin glass behavior in spinel compound CoGa_2O_4 . *Journal of Materials Science: Materials in Electronics* **32**, 14592-14600 (2021).
29. S. Koseki, N. Matsunaga, T. Asada, M. W. Schmidt, M. S. Gordon, Spin-Orbit coupling constants in atoms and ions of transition elements: comparison of effective core potentials, model core potentials, and all-electron methods. *The Journal of Physical Chemistry A* **123**, 2325-2339 (2019).
30. M. M. Bordelon *et al.*, Frustrated Heisenberg $J_1 - J_2$ model within the stretched diamond lattice of LiYbO_2 . *Physical Review B* **103**, 014420 (2021).
31. L. Ge *et al.*, Spin order and dynamics in the diamond-lattice Heisenberg antiferromagnets CuRh_2O_4 and CoRh_2O_4 . *Physical Review B* **96**, 064413 (2017).
32. K. Guratinder *et al.*, Magnetic order and exchange coupling in the frustrated diamond-lattice antiferromagnet MnSc_2Se_4 . *Physical Review B* **105**, 174423 (2022).
33. N. D. Kelly *et al.*, Magnetism on the stretched diamond lattice in lanthanide orthotantalates. *Physical Review Materials* **6**, 044410 (2022).
34. W.-L. Lee, S. Watauchi, V. L. Miller, R. J. Cava, N. P. Ong, Dissipationless anomalous hall current in the ferromagnetic spinel $\text{CuCr}_2\text{Se}_{4-x}\text{Br}_x$. *Science* **303**, 1647-1649 (2004).

35. C. H. Lee *et al.*, Multistage development of anisotropic magnetic correlations in the Co-based honeycomb lattice $\text{Na}_2\text{Co}_2\text{TeO}_6$. *Physical Review B* **103**, 214447 (2021).
36. M. Songvilay *et al.*, Kitaev interactions in the co honeycomb antiferromagnets $\text{Na}_3\text{Co}_2\text{SbO}_6$ and $\text{Na}_2\text{Co}_2\text{TeO}_6$. *Physical Review B* **102**, 224429 (2020).
37. X. Liu, H.-Y. Kee, Non-Kitaev versus Kitaev honeycomb cobaltates. *Physical Review B* **107**, 054420 (2023).
38. P. Chanlert, N. Kurita, H. Tanaka, M. Kimata, H. Nojiri, Collective and local excitations in $\text{Ba}_2\text{CoTeO}_6$: A composite system of a spin-1/2 triangular-lattice Heisenberg antiferromagnet and a honeycomb-lattice J_1 - J_2 Ising antiferromagnet. *Physical Review B* **96**, 064419 (2017).
39. H. S. Nair *et al.*, Short-range order in the quantum XXZ honeycomb lattice material $\text{BaCo}_2(\text{PO}_4)_2$. *Physical Review B* **97**, 134409 (2018).
40. P. A. Maksimov *et al.*, Cobalt-based pyroxenes: A new playground for Kitaev physics. *Proceedings of the National Academy of Sciences* **121**, e2409154121 (2024).
41. K. Dey, S. Majumdar, S. Giri, Ferroelectricity in spiral short-range-ordered magnetic state of spinel MnCr_2O_4 : Significance of topological frustration and magnetoelastic coupling. *Physical Review B* **90**, 184424 (2014).
42. A. Kalz, A. Honecker, S. Fuchs, T. Pruschke, Phase diagram of the Ising square lattice with competing interactions. *The European Physical Journal B* **65**, 533-537 (2008).
43. Y. Haraguchi, T. Ohnoda, A. Matsuo, K. Kindo, H. A. Katori, Perfect kagome-lattice antiferromagnets with $J_{\text{eff}} = 1/2$: The Co^{2+} analogs of the copper minerals volborthite and vesignieite. *Physical Review B* **106**, 214421 (2022).
44. G. Lin *et al.*, Field-induced quantum spin disordered state in spin-1/2 honeycomb magnet $\text{Na}_2\text{Co}_2\text{TeO}_6$. *Nature communications* **12**, 5559 (2021).
45. F. Lloret, M. Julve, J. Cano, R. Ruiz-García, E. Pardo, Magnetic properties of six-coordinated high-spin cobalt (II) complexes: Theoretical background and its application. *Inorganica Chimica Acta* **361**, 3432-3445 (2008).
46. H. Ueda, H. A. Katori, H. Mitamura, T. Goto, H. Takagi, Magnetic-Field Induced Transition to the 1/2 Magnetization Plateau State in the Geometrically Frustrated Magnet CdCr_2O_4 . *Physical review letters* **94**, 047202 (2005).
47. Y. Long, Q. Liu, Y. Lv, R. Yu, C. Jin, Various $3d$ - $4f$ spin interactions and field-induced metamagnetism in the Cr^{5+} system DyCrO_4 . *Physical Review B* **83**, 024416 (2011).
48. S. Gupta, R. Rawat, K. G. Suresh, Large field-induced magnetocaloric effect and magnetoresistance in ErNiSi . *Applied Physics Letters* **105**, (2014).
49. R. Zhong, T. Gao, N. P. Ong, R. J. Cava, Weak-field induced nonmagnetic state in a Co-based honeycomb. *Science advances* **6**, eaay6953 (2020).
50. P. A. Maksimov *et al.*, Ab initio guided minimal model for the “Kitaev” material $\text{BaCo}_2(\text{AsO}_4)_2$: Importance of direct hopping, third-neighbor exchange, and quantum fluctuations. *Physical Review B* **106**, 165131 (2022).
51. L. P. Regnault, C. Boullier, J. E. Lorenzo, Polarized-neutron investigation of magnetic ordering and spin dynamics in $\text{BaCo}_2(\text{AsO}_4)_2$ frustrated honeycomb-lattice magnet. *Heliyon* **4**, (2018).
52. T. Halloran *et al.*, Geometrical frustration versus Kitaev interactions in $\text{BaCo}_2(\text{AsO}_4)_2$. *Proceedings of the National Academy of Sciences* **120**, e2215509119 (2023).

53. S. Mukherjee, G. Manna, P. Saha, S. Majumdar, S. Giri, Ferroelectric order with a linear high-field magnetoelectric coupling in $\text{Na}_2\text{Co}_2\text{TeO}_6$: A proposed Kitaev compound. *Physical Review Materials* **6**, 054407 (2022).
54. W. Yao, K. Iida, K. Kamazawa, Y. Li, Excitations in the ordered and paramagnetic states of honeycomb magnet $\text{Na}_2\text{Co}_2\text{TeO}_6$. *Physical Review Letters* **129**, 147202 (2022).
55. S. H. Baek *et al.*, Evidence for a field-induced quantum spin liquid in $\alpha\text{-RuCl}_3$. *Physical review letters* **119**, 037201 (2017).
56. A. Steppke *et al.*, Nuclear contribution to the specific heat of $\text{Yb}(\text{Rh}_{0.93}\text{Co}_{0.07})_2\text{Si}_2$. *physica status solidi (b)* **247**, 737-739 (2010).
57. P. Blaha, K. Schwarz, G. K. H. Madsen, D. Kvasnicka, J. Luitz, wien2k. *An augmented plane wave+ local orbitals program for calculating crystal properties* **60**, (2001).
58. P. Giannozzi *et al.*, QUANTUM ESPRESSO: a modular and open-source software project for quantum simulations of materials. *Journal of physics: Condensed matter* **21**, 395502 (2009).
59. S. Maintz, V. L. Deringer, A. L. Tchougréeff, R. Dronskowski, LOBSTER: A tool to extract chemical bonding from plane-wave based DFT. (2016).
60. R. Nelson *et al.*, LOBSTER: Local orbital projections, atomic charges, and chemical-bonding analysis from projector-augmented-wave-based density-functional theory. *Journal of Computational Chemistry* **41**, 1931-1940 (2020).
61. R. Dronskowski, P. E. Blöchl, Crystal orbital Hamilton populations (COHP): energy-resolved visualization of chemical bonding in solids based on density-functional calculations. *The Journal of Physical Chemistry* **97**, 8617-8624 (1993).
62. V. L. Deringer, A. L. Tchougréeff, R. Dronskowski, Crystal orbital Hamilton population (COHP) analysis as projected from plane-wave basis sets. *The journal of physical chemistry A* **115**, 5461-5466 (2011).
63. J. Rodríguez-Carvajal, Recent advances in magnetic structure determination by neutron powder diffraction. *Physica B: Condensed Matter* **192**, 55-69 (1993).
64. J. Perl, J. Shin, J. Schümann, B. Faddegon, H. Paganetti, TOPAS: an innovative proton Monte Carlo platform for research and clinical applications. *Medical physics* **39**, 6818-6837 (2012).
65. A. A. Coelho, TOPAS and TOPAS-Academic: an optimization program integrating computer algebra and crystallographic objects written in C++. *Journal of Applied Crystallography* **51**, 210-218 (2018).
66. C. C. Gu *et al.*, Field-driven quantum criticality in the spinel magnet ZnCr_2Se_4 . *Physical Review Letters* **120**, 147204 (2018).
67. S. Park *et al.*, Interactions in the bond-frustrated helimagnet ZnCr_2Se_4 investigated by NMR. *Scientific Reports* **9**, 16627 (2019).
68. H. Cho *et al.*, Dynamic spin fluctuations in the frustrated A-site spinel CuAl_2O_4 . *Physical Review B* **102**, 014439 (2020).
69. R. Nirmala *et al.*, Spin glass behavior in frustrated quantum spin system CuAl_2O_4 with a possible orbital liquid state. *Journal of Physics: Condensed Matter* **29**, 13LT01 (2017).
70. P. C. Müller, C. Ertural, J. Hempelmann, R. Dronskowski, Crystal orbital bond index: Covalent bond orders in solids. *The Journal of Physical Chemistry C* **125**, 7959-7970 (2021).

71. D. M. Korotin, V. V. Mazurenko, V. I. Anisimov, S. V. Streltsov, Calculation of exchange constants of the Heisenberg model in plane-wave-based methods using the Green's function approach. *Physical Review B* **91**, 224405 (2015).
72. X. Huai *et al.*, Noncentrosymmetric Triangular Magnet CaMnTeO₆: Strong Quantum Fluctuations and Role of s^0 versus s^2 Electronic States in Competing Exchange Interactions. *Advanced Materials*, 2313763 (2024).
73. J. Z. Ma *et al.*, Spin fluctuation induced Weyl semimetal state in the paramagnetic phase of EuCd₂As₂. *Science advances* **5**, eaaw4718 (2019).
74. J. A. M. Paddison *et al.*, Hidden order in spin-liquid Gd₃Ga₅O₁₂. *Science* **350**, 179-181 (2015).